SEMICONDUCTOR SUPERLATTICES WITH SMALL BAND OFFSETS

G. YANG, L.A. LEWANDOWSKI*, J.K. FURDYNA

Department of Physics, University of Notre Dame, Notre Dame, IN 46556, USA

AND L.R. RAM-MOHAN

Departments of Physics, Electrical and Computer Engineering
Worcester Polytechnic Institute, Worcester, MA 01609, USA

Optical transitions in small band offset superlattices are studied within the framework of the nearly free electron approximation, in which the weak superlattice potential is treated as a perturbation. Interband selection rules are derived for transitions involving conduction and valence band states at the superlattice Brillouin zone center and the zone edge. It is found that a number of new transitions can occur in such small-offset superlattices due to wave function mixing of different subband states. The effect of the effective mass on the optical transitions is also discussed. The theory is used to explain the results observed in magneto-optical absorption experiment in $ZnSe/Zn_{1-x}Mn_xSe$ small-offset superlattices. Furthermore, the nearly free electron formulation is found to be in excellent agreement with rigorous multi-band numerical calculation on superlattices involving small band offsets.

PACS numbers: 78.66.–w

1. Introduction

Electronic properties of semiconductor superlattices (SLs) are determined primarily by the differences in the conduction and valence band edges at the interfaces between constituent layers. (i.e., the so-called "band offsets"). Studies of SLs carried out so far have focused primarily on structures with relatively large band offsets (for a comprehensive discussion of electronic band structure of quantum wells and superlattices, see Ref. [1]), where electrons and holes are strongly localized by the confining potentials of the wells. Motion of the confined states along the

---

*Present address: Department of Therapeutic Radiology, Radiation Oncology, University of Minnesota School of Medicine, Minneapolis, MN 55405, USA.

growth direction is in such structures quantized into fairly narrow "mini-bands", which are often treated simply as discrete energy levels. Because of such selective quantization of motion in the growth direction — as compared to motion in the layer plane — quantum wells and superlattices described by large band offsets behave essentially as two-dimensional media.

In contrast, the present paper will focus specifically on SLs in which the band offset is *small* in both bands. Our interest in such structures is motivated by the fact that the analysis of SLs with small offsets will permit us to describe the physical phenomena which occur in the region where the superlattice *just begin to form*. This transition region, where the SL transforms from a 3D to a 2D medium, may be referred to as the *intermediate dimensionality regime.*

While such a regime of dimensional transition is of considerable fundamental interest, it is surprising that so far little attention has been devoted to this subject[†] [2, 3]. Our objective, then, is to carry out a detailed investigation of the electronic band structure of SLs with very small offsets in various geometries, with special attention to optical transitions which result from such band structure. We will show that, in sharp contrast with large-band-offset SLs, in SLs with small offsets the energy subbands become very wide and are separated by very narrow minigaps. Such subbands are localized *not* by confining potentials, but by *interference* effects among Bragg-reflected electron waves. Using the nearly free electron (NFE) approximation [4], we will derive analytic expressions for the energies, the wave functions, and the effective masses at the minigaps of small band-offset SLs. We will then use these results to discuss the optical properties of such structures, with emphasis on selection rules and optical transition intensities. As will be seen, a large number of new optical transitions will emerge when the band offsets are small due to the wave function mixing of different subbands. Furthermore, transitions which occur at the Brillouin zone center can be readily distinguished in this regime from those occurring at the zone edges.

The organization of the paper is as follows. In Sec. 2, we identify some of the real physical systems in which small-offset processes can be observed and studied. In Sec. 3, we present the NFE approximation by which we approach the problem of small-band-offset SLs, and we describe the basic properties of their band structure and wave functions in analytical form. In Sec. 4 we discuss the optical behavior of small-offset SLs. In Sec. 5 we compare the results calculated with the NFE approximation (which, being analytical, has the advantages of keeping the physics in focus) and those calculated numerically using a full 8-band $k \cdot p$ model. These comparisons are also used to establish the limits of applicability of the analytical NFE formulation.

2. Small-offset superlattices
2.1. Are small-offset structures realistic?

We begin by defining the small-offset SL. The term "small-band offset" is relative, and will depend on many parameters, such as the widths of wells and

---

[†]Some of the unique properties of small-offset superlattices have been pointed out in Ref. [2]. Indeed, the present study was largely motivated by the insights and experimental observations reported in that work.

barriers, and on the effective masses. This will be discussed quantitatively at the end of Sec. 3. As a practical guide, however, we will define the offset as small when it is below about 3% of the energy gap of the barrier material.

To fabricate a small-offset superlattice, one obvious approach is to use two materials that differ only slightly from one another. $GaAs/Ga_{0.95}Al_{0.05}As$ and $ZnSe/Zn_{0.95}Cd_{0.05}Se$ can be safely expected to have very small offsets. Another procedure is to exploit "bowing" of the energy gap with composition found in certain ternary alloys. For example, the energy gap of $Zn_{1-x}Mn_xSe$ first decreases with x, and then increases rapidly to values far exceeding the band gap of ZnSe [5]. Thus there exists a Mn concentration x ($x \approx 0.05$) where the $Zn_{1-x}Mn_xSe$ and the ZnSe gaps are exactly equal. Since $ZnSe/Zn_{1-x}Mn_xSe$ is a common-anion combination, the valence bands are expected to remain closely aligned, and so then must be the conduction bands at this specific concentration [2].

A much wider spectrum of small-offset SLs can be fabricated using ternary alloys as both constituents. For example, combinations of $Cd_{1-x}Zn_xTe/Cd_{1-y}Mg_yTe$, $Zn_{1-x}Mn_xTe/Zn_{1-y}Mg_yTe$, or $Zn_{1-x}Mn_xSe/Zn_{1-y}Mg_ySe$ with appropriately chosen values of x and y will result in small (or even zero) offset SLs [3]. The point here is not to list all such possible combinations, but rather to demonstrate that small-offset SLs can indeed be realized in practice.

We finally note, on intuitive grounds, that SLs with very narrow wells can also be viewed as small offset SLs even when the absolute value of the band offset is large. States in such SLs move up in energy as the well width becomes narrower. In the limit of very narrow wells (say, $L < 25$ Å or so, depending on the effective mass) the ground states of the SL will be "pushed up" very close to the top of the well. We shall see that in this situation (which includes the important family of *short-period SLs*) the SL will also behave as a "small-offset" system. These plausible arguments will be demonstrated at the end of Sec. 3.4.

2.2. Tunable band-offset structures

The effect of any parameter on the physical properties of a system can best be studied by varying that parameter. Thus in the case of small-offset structures, one could grow a series of $GaAs/Ga_{1-x}Al_xAs$ SLs for different values of x (e.g., $x = 0.01, 0.02, 0.03$, etc.). The fabrication of specimens with offsets progressing in such minute steps (on the scale of 5 meV or so) is, however, quite problematic. Even if we could control x to this degree, it is unlikely that one would be able to control the *geometry* of repeated growths to the precision required by this very fine progression of energies.

It would be ideal to "tune" the offset *in the same structure*. The unique properties of *diluted magnetic semiconductors* (DMSs) provide just such an opportunity, since their band gap undergoes enormous Zeeman splittings when an external magnetic field is applied [6]. For example, the $Zn_{1-x}Mn_xSe$ band gap can be varied by as much as 100 meV in a magnetic field of 5 tesla. This feature can be directly exploited for varying ("tuning") the band offset in SLs comprised of alternating DMS and non-DMS layers, simply by applying a magnetic field. The phenomenon of such band offset tuning has in fact already been experimentally observed in many DMS SLs, e.g., in $Zn_{1-x}Mn_xSe/ZnSe$ [7], $Zn_{1-x}Fe_xSe/ZnSe$ [8]

and $Cd_{1-x}Mn_xTe/CdTe$ [9]. The band-offset in all these structures can be easily tuned by a magnetic field over several tens of meV.

3. Electronic structure of superlattices with small band offsets

3.1. Energy subbands and wave functions: first-order perturbation

We begin by considering a single band of a SL (e.g., the conduction band). The behavior of an electron in this structure is determined by the Schrödinger equation,

$$H\psi(z) = \left(-\frac{\hbar^2}{2m^*}\frac{d^2}{dz^2} + V(z)\right)\psi(z) = E\psi(z), \tag{1}$$

where H is the Hamiltonian, m^* is the effective mass, E represents the eigenenergies of the system, and $V(z)$ is the periodic superlattice potential with a period L along the z-direction (i.e., the growth axis of the SL). Such a potential can be expanded as a complex Fourier series,

$$V(z) = \sum_{n=-\infty}^{\infty} V_n e^{i(2\pi/L)nz}, \tag{2}$$

where n is an integer, and the Fourier coefficients V_n are given by

$$V_n = \frac{1}{L}\int_0^L V(z)e^{-i(2\pi/L)nz}\,dz. \tag{3}$$

The most commonly encountered SLs are those with *rectangular* potential profiles. If the origin of the z-axis is taken to be the center of one of the wells, we find from Eq. (3) that

$$V_n = -\frac{V}{n\pi}\sin\left(n\pi L_w/L\right), \tag{4}$$

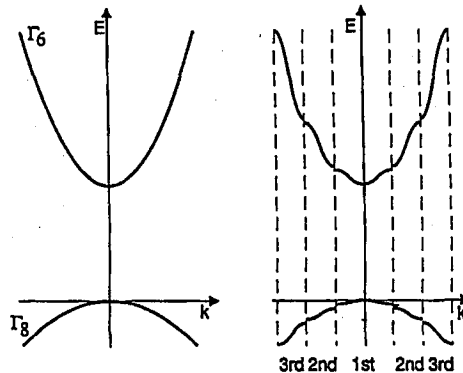where L_w is the width of the well, and V is its depth.

Fig. 1.   Plot of energy E vs. wave vector k for electrons and heavy holes in a bulk semiconductor (left panel) and in a superlattice with a *weak* periodic potential (right panel).

In a typical bulk zinc blende semiconductor, a free electron or hole has a parabolic dispersion relation in any direction, as shown in the left panel of Fig. 1. When a weak periodic potential is turned on in the z-direction (thus forming a small-offset SL), the E vs. k_z dispersion relation remains essentially the same, except that there appear small gaps (minigaps) in narrow regions close to the SL Bragg planes, i.e., corresponding to the SL reciprocal lattice vectors. The dispersion curves are then broken into segments belonging to consecutive SL Brillouin zones, as shown in the right panel in Fig. 1. The dispersion curves in Brillouin zones other than the first can then be "folded" into the first zone by adding a reciprocal lattice vector appropriate for the SL. The regions of k with highest densities of states (i.e., those important in optical transitions) correspond to the center and to the edges of the Brillouin zone, i.e., to $k_z = \pm n\pi/L$ of the original free electron band. We shall, therefore, focus on the energies and wave functions of states at the zone center and zone edges.

In the NFE approximation, it is assumed that $V(z)$ is small in comparison with the kinetic energy term. We can thus treat $V(z)$ as a perturbation. To first-order, the energy at $k = \pm n\pi/L$ has *two* values, given by [10, 11]

$$E_{n,\pm} = T_n \pm |V_n|, \tag{5}$$

where $T_n = \hbar^2 n^2 \pi^2 / (2m^* L^2)$. This then results in the formulation of minigaps, as shown in Fig. 1, the magnitude of the n-th gap being proportional to the n-th Fourier component of the SL potential [12],

$$E_{g,n} = 2|V_n|. \tag{6}$$

Standard perturbation analysis also gives the wave functions associated with the upper $(E_{n,+})$ and the lower $(E_{n,-})$ energy states, given respectively by [3, 12]

$$\psi_{n,+}^{(0)}(z) = \frac{\sqrt{2}e^{-i\theta_n}}{\sqrt{L}} \cos\left(\frac{n\pi z}{L} + \theta_n\right),$$

$$\tag{7}$$

$$\psi_{n,-}^{(0)}(z) = \frac{\sqrt{2}ie^{-i\theta_n}}{\sqrt{L}} \sin\left(\frac{n\pi z}{L} + \theta_n\right).$$

The phase angle θ_n in Eq. (7) is determined by the relation $e^{2i\theta_n} = V_n/|V_n|$, which depends on the geometry of a given superlattice.

For SLs with a rectangular potential profile, we see from Eq. (4) that V_n is a real quantity. Thus the value of θ_n must be either 0 or $\pi/2$. The two states associated with the n-th gap will then have $\cos(n\pi z/L)$ and $\sin(n\pi z/L)$ dependences. Which of these corresponds to the higher, and which to the lower-lying state at the minigaps, will be determined by the specific barrier and well dimensions.

The effective masses associated with the n-th zone edge are given by the very convenient analytic expressions derived in Appendix B

$$m_{n+}^* = -m_{n-}^* = \frac{m^*|V_n|}{2T_n} = \frac{m^* E_{g,n}}{4T_n}, \tag{8}$$

where, as before, the $+$ and $-$ subscripts refer to the higher and lower-lying state. This means that the effective mass at the n-th minigap is directly proportional to the width of that minigap.

It is easy to see from Eq. (4) that, depending on the relationship of L_w to L, V_n can vanish for certain n. In this case, according to Eq. (6), the minigap at $k_z = \pm n\pi/L$ will also vanish. This result is a consequence of first-order perturbation theory. Second-order perturbation analysis will show, however, that the minigaps do not completely vanish at the condition $V_n = 0$. We have derived in Appendices A and B the expressions for the minigap widths, wave functions, and effective masses associated with the $V_n = 0$ condition. It is noted that the minigap widths corresponding to $V_n = 0$ are indeed very small (see Appendix A); and the magnitudes of the effective masses are, accordingly, much smaller than the masses associated with minigaps which are open in first-order calculation (i.e., when $V_n \neq 0$; see Appendix B). The densities of states associated with points in the Brillouin zone corresponding to n for which $V_n = 0$ are then extremely small, and optical transitions occurring at these points are expected to be correspondingly weak.

As stated above, the conditions for which $V_n = 0$ depends on the SL geometry. Before proceeding further, we identify the specific cases for which $V_n = 0$ (i.e., which minigaps correspond to weak optical transitions):

(a) When $L_w = L_b$ ($L_w/L = 1/2$), we see immediately that V_n will vanish (and thus minigaps will close in first order) for all even values of n;

(b) When $L_b = 2L_w$ ($L_w/L = 1/3$) or $L_w = 2L_b$ ($L_w/L = 2/3$), first-order minigaps will close for $n = 3, 6, 9\ldots$, and higher multiples of 3;

(c) When $L_b = 3L_w$ ($L_w/L = 1/4$) or $L_w = 3L_b$ ($L_w/L = 3/4$), first-order minigaps will close for $n = 4, 8, 12, \ldots$ etc.;

(d) When $L_w/L = 1/5, 2/5, 3/5$, or $4/5$, the lowest minigap to close will be for $n = 5, \ldots$ and so on.

In general, the thinner the well or the barrier, the higher the value of n for the lowest vanishing minigap. Because of the small density of states at such minigaps, we will not consider them in the context of optical transitions, restricting ourselves to these gaps which are open in first-order perturbation analysis. Here it is important to note that there is no geometry for which the *lowest* minigap ($n = 1$) could go to zero in first-order perturbation, since for that to happen, Eq. (4) would require that $L_w = 0$ or $L_w = L$, a condition under which the SL itself would disappear.

3.2. Illustrative example: $L_w = L_b$

As a specific illustration of first-order perturbation results, consider a SL with wells and barriers of equal width, $L_w = L_b$, i.e., $L = 2L_w$. As already stated, we choose the origin $z = 0$ to be at the center of one of the wells. Using $L_w = L_b$ in Eq. (4), we get

$$
V_n = \begin{cases} -V/(n\pi) & n = 1, 5, 9, 13, \ldots \\ V/(n\pi) & n = 3, 7, 11, 15, \ldots \\ 0 & n = 2, 4, 6, 8, 10, \ldots \end{cases} \tag{9}
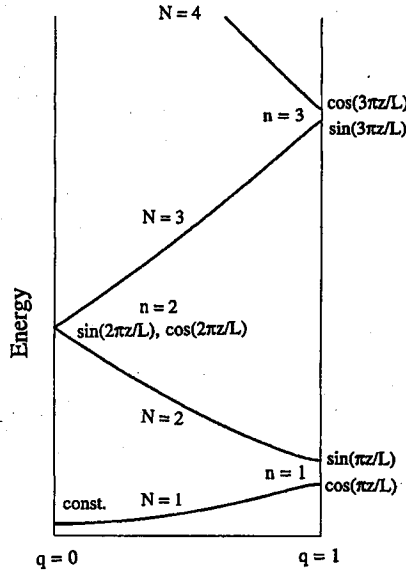$$

Fig. 2. Reduced-zone representation of band structure for the conduction band of a superlattice with $L_w = L_b$, obtained by first-order perturbation analysis. The SL wave vector is represented by q. Wave functions corresponding to zone center ($q = 0$) and zone edge ($q = 1$) states of the superlattice are also indicated. Note that for the case $L_w = L_b$ the minigaps are closed for all even values of n in the first-order calculation, as seen explicitly for $n = 2$.

First-order perturbation analysis thus leads to the vanishing of minigaps when n is even (via Eq. (4)), while the minigaps for odd n are finite, but get progressively smaller with increasing n, yielding the picture of the band structure shown in Fig. 2 (where the SL wave vector is denoted by q, and the minigap at $k_z = \pm n\pi/L$ in the extended zone is denoted by the index n).

We can now determine the wave functions for the finite (odd n) minigaps. We recall that for a rectangular potential the wave functions are pure sines and cosines of argument $(n\pi z/L)$. Their ordering (i.e., whether the upper state will be cosine-like or sine-like) depends on the *sign* of V_n, which determines the phase θ_n in Eq. (7). If $V_n > 0$ (i.e., for $n = 3, 7, 11, \ldots$ as shown in Eq. (9)), $\theta_n = 0$, and Eq. (7) becomes

$$\psi_{n+} = \frac{\sqrt{2}}{\sqrt{L}} \cos(n\pi z/L), \qquad \psi_{n-} = i\frac{\sqrt{2}}{\sqrt{L}} \sin(n\pi z/L). \qquad (10)$$

On the other hand, when $V_n < 0$ (i.e., for $n = 1, 5, 9, \ldots$), $\theta_n = \pi/2$, yielding

$$\psi_{n+} = i\frac{\sqrt{2}}{\sqrt{L}} \sin(n\pi z/L), \qquad \psi_{n-} = \frac{\sqrt{2}}{\sqrt{L}} \cos(n\pi z/L). \qquad (11)$$

For even n, ($V_n = 0$), second-order perturbation must be applied to obtain $E_{g,n}$, as discussed in Appendices A and B. For example, it is shown in Appendix A that the minigap for $n = 2$ is $V^2/(4T_2)$, which is extremely small (smaller than
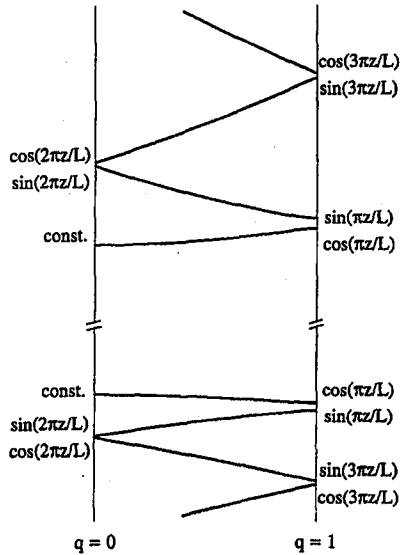
Fig. 3. Band structure for the same SL as that discussed in Fig. 2, illustrating that the closed first-order gaps are "opened" by second-order perturbation theory.

the higher-lying minigaps for odd n), but nevertheless finite. The wave functions for the upper and lower extrema associated with this gap are, respectively,

$$\psi_{2,+} = \frac{\sqrt{2}}{\sqrt{L}} \cos(2\pi z/L), \qquad \psi_{2,-} = \frac{\sqrt{2}}{\sqrt{L}} \sin(2\pi z/L), \tag{12}$$

as shown by Eq. (A16). Figure 3 shows the subband structure with proper order of the wave functions at the minigaps for the case of $L_w = L_b$.

3.3. Wave function mixing: second-order perturbation

Wave functions play a central role in determining the selection rules for optical transitions, since the transition intensity is determined by the wave function overlap between the initial and the final states. When the band offset is very small, the $\sin(n\pi z/L)$ and $\cos(n\pi z/L)$ functions obtained from first-order perturbation provide a good description for wave functions of the states at the n-th minigap. However, we will show next that, as the offset increases (although still satisfying the "smallness" criteria discussed in Sec. 3.4), it will progressively bring about admixtures from other nearby subband states into the wave function under consideration.

To discuss such mixing, we start by taking $\sin(n\pi z/L)$ and $\cos(n\pi z/L)$ functions as new basis functions at the n-th minigap. We then include the second-order contributions to these wave functions by means of second-order perturbation theory. Let us first consider the even parity (cosine) state. Since we have chosen the center of the well as the origin of the z-axis, the superlattice potential is characterized by inversion symmetry. Thus

$$\langle \cos(n'\pi z/L)|V|\sin(n\pi z/L)\rangle = 0, \tag{13}$$

i.e, the wave functions with different parity will not mix. So for the even-parity state

$$\psi_n = A_n \frac{\sqrt{2}}{\sqrt{L}}$$

$$\times \left[\cos(n\pi z/L) + \frac{2}{L} \sum_{n' \neq n} \frac{\langle \cos(n'\pi z/L)|V|\cos(n\pi z/L)\rangle}{T_n - T_{n'}} \cos(n'\pi z/L) \right]. \quad (14)$$

Using Eq. (3), we then have

$$\psi_n = A_n \frac{\sqrt{2}}{\sqrt{L}}$$

$$\times \left[\cos(n\pi z/L) + \sum_{n' \neq n} \frac{\mathrm{Re}\left(V_{(n'-n)/2} + V_{(n'+n)/2}\right)}{T_n - T_{n'}} \cos(n'\pi z/L) \right]. \quad (15)$$

Letting $n' - n/2 = m$, where $m = \pm 1, \pm 2, \ldots$, Eq. (15) becomes

$$\psi_n = A_n \frac{\sqrt{2}}{\sqrt{L}} \left[\cos(n\pi z/L) + \sum_{m \neq 0} \frac{\mathrm{Re}\left(V_m + V_{m+n}\right)}{T_n - T_{n+2m}} \cos((n+2m)\pi z/L) \right]. \quad (16)$$

Similarly, for the odd parity state, we obtain

$$\psi'_n = A'_n \frac{\sqrt{2}}{\sqrt{L}}$$

$$\times \left[\sin(n\pi z/L) + \sum_{m \neq 0} \frac{\mathrm{Re}(V_m + V_{m+n})}{T_n - T_{n+2m}} \sin((n+2m)\pi z/L) \right]. \quad (17)$$

Therefore, as the offset increases, it progressively brings about admixtures from neighboring subband states of the *same parity*, as shown by the second term on the right.

As an example, we refer once again to the case of a rectangular potential with $L_w = L_b$. We can now obtain the wave functions to second order for such a system, for all minigap extrema. We illustrate this explicitly for states at the zone center ($q = 0$). For $n = 0$, we obtain

$$\psi_0 = \frac{A_0}{\sqrt{L}} \left[1 + \frac{2V}{\pi T_2} \cos(2\pi z/L) \right], \quad (18)$$

where the normalization factor A_0 is $\{1 + 2[V/(\pi T_2)]^2\}^{-1/2}$.

For $n = 2$, we obtain

$$\psi_{2,+} = \frac{\sqrt{2}}{\sqrt{L}} A_{2,+} \left[\cos(2\pi z/L) - \frac{V}{\pi T_2} + \frac{4V}{9\pi T_2} \cos(4\pi z/L) \right] \quad (19)$$

and

$$\psi_{2,-} = \frac{\sqrt{2}}{\sqrt{L}} A_{2,-} \left[\sin(2\pi z/L) - \frac{2V}{9\pi T_2} \sin(4\pi z/L) \right], \quad (20)$$

TABLE I

Wave functions for several lowest conduction subband states, showing admixtures* from the nearest neighboring states.

State	Wave function
$e1_0$	$1 + 2\delta_c \cos(2\pi z/L)$
$e1_1$	$\cos(\pi z/L) + \frac{1}{2}\delta_c \cos(3\pi z/L)$
$e2_1$	$\sin(\pi z/L) - \frac{1}{2}\delta_c \sin(3\pi z/L)$
$e2_0$	$\sin(2\pi z/L) - \frac{2}{9}\delta_c \sin(4\pi z/L)$
$e3_0$	$\cos(2\pi z/L) - \delta_c + \frac{4}{9}\delta_c \cos(4\pi z/L)$
$e3_1$	$\sin(3\pi z/L) + \frac{1}{2}\delta_c \sin(\pi z/L) - \frac{1}{4}\delta_c \sin(5\pi z/L)$
$e4_1$	$\cos(3\pi z/L) - \frac{1}{2}\delta_c \cos(\pi z/L) + \frac{1}{4}\delta_c \cos(5\pi z/L)$

*Admixture parameter $\delta_c = V^c/(\pi T_2^c)$.

where $A_{2,+} = \{1 + 2[V/(\pi T_2)]^2 + [4V/(9\pi T_2)]^2\}^{-1/2}$, and
$A_{2,-} = \{1 + [2V/(\pi T_2)]^2\}^{-1/2}$.

It should be noted that, in deriving Eqs. (18–20), only admixtures from the *nearest* neighboring subbands to the first-order wave functions are included. When the offset is small (the term "small" will be defined in the next section), admixtures from the more remote subbands rapidly decreases with energy separation, and can be neglected. We illustrate this by Table I, which lists wave functions for several lowest conduction band states, including the admixtures from the nearest neighboring states. In the table, we use the following notation. The subband states are denoted by eN_q, where e stands for "electron", N represents the N-th subband, and q is the SL wave vector. The parameter δ_c is defined as $V^c/(\pi T_2^c)$, where the superscript "c" stands for conduction band, and V and T_2 have been defined earlier. The wave functions of the corresponding heavy-hole subband states at $q = 0$ and $q = 1$ have the same form as those given in Table I, with δ_c replaced by $\delta_v = V^v/(\pi T_2^v)$, the superscript "v" denoting heavy-hole valence band parameters.

3.4. Conditions for small band offset

In discussing SLs with small band offsets, the term "small" is relative, and must be defined more precisely. We do this for SLs with rectangular potentials, where the Fourier coefficients are always real quantities. By inspection of Eqs. (16) and (17), we note that the following condition must be satisfied for the perturbation theory to be applicable:

$$\left| \frac{V_m \pm V_{n+m}}{T_{n+2m} - T_n} \right| \ll 1. \tag{21}$$

This condition will be different for different states, becoming more relaxed as n increases. Thus, if we define the "small-offset" criterion for low-lying states, it will be automatically satisfied for *all* states.

It is easy to see that the smallest value of the denominator $T_{n+2m} - T_n$ in Eq. (21) (i.e., that corresponding to the lowest-lying state, $n = 0$) is T_2. At the

same time the numerator $V_m \pm V_{n+m}$ decreases with n (see Eq. (4)), so that its largest value is $2V_1$. The most stringent form of Eq. (21) is therefore

$$\frac{2|V_1|}{T_2} \ll 1. \tag{22}$$

If Eq. (22) is satisfied, Eq. (21) is automatically satisfied for all n and m.

We will therefore use Eq. (22) as our criterion for defining the offset as "small", and we now examine this condition in greater detail. For a rectangular potential profile

$$|V_1| = \frac{V}{\pi} \left| \sin\left(\pi L_w/L\right) \right|. \tag{23}$$

Substituting Eq. (23) into Eq. (22) leads to the following condition:

$$\frac{2V \left| \sin\left(\pi L_w/L\right) \right|}{\pi T_2} \ll 1. \tag{24}$$

Since $T_2 = (2\pi\hbar)^2/(2m^* L^2)$, we then have the small-offset condition expressed in the compact form

$$V \ll \frac{\hbar^2 \pi^3}{m^*} \frac{1}{L^2} \frac{1}{\left| \sin\left(\pi L_w/L\right) \right|}. \tag{25}$$

Now we note that $|\sin(\pi L_w/L)|$ has its highest value for $L_w = L_b$, resulting in the most stringent inequality for small offsets,

$$V \ll \frac{\hbar^2 \pi^3}{m^*} \frac{1}{L^2}. \tag{26}$$

This can be expressed in units of meV as

$$V \ll 23.5 \left(\frac{m_0}{m^*}\right) \left(\frac{100}{L}\right)^2 \text{ [meV]} \equiv V_{\text{cr}}, \tag{27}$$

where m_0 is the free electron mass, L is expressed in Å, and we label the right-hand-side as the critical value, V_{cr}.

We use Eq. (27) to give a numerical estimate of a "small-offset". Using 100 Å as a representative SL period, and $m^* = 0.15m_0$ as a typical electron effective mass for wide-gap II–VI semiconductors, we obtain the V_{cr} in Eq. (27) to be 157 meV. Taking 25% of that value as sufficient for the perturbation calculation to hold, a SL with a band offset of 40 meV or less can safely be regarded as a "small-offset" SL. This is consistent with our "working" hypothesis expressed earlier that the offset may be regarded as small when it is below about 3% of the energy gap of the barrier material. We will show later by exact numerical calculations that even SLs whose offsets significantly exceed this criterion are still satisfactorily described by the analytic expressions derived via the perturbation approach.

Several additional insights follow from Eq. (25). First, the smaller the effective mass, or the shorter the SL *period*, the higher can be the actual value of the offset V satisfying the perturbation condition. And second, we note that as L_w departs from $L/2$ value, $|\sin(\pi L_w/L)|$ in the denominator of Eq. (25) will decrease. Thus the narrower the thickness of *either* the wells *or* the barriers, the higher can be the actual value of V satisfying the small-offset condition. This justifies the "intuitive" comments made earlier, at the end of Sec. 2.1.

TABLE II

Critical band offset values V_{cr} for small band-offset SLs.

L_w (in Å)	L_b (in Å)	CB ($m_c = 0.15m_0^*$)	VB ($m_v = 0.6m_0^*$)
100	100	38 meV	9 meV
75	75	88 meV	22 meV
50	50	157 meV	39 meV
25	25	527 meV	157 meV
33	67	182 meV	45 meV
25	75	222 meV	55 meV
10	90	507 meV	127 meV
67	33	182 meV	45 meV
75	25	222 meV	55 meV
90	10	507 meV	127 meV

We illustrate these features in Table II, which shows the estimates of V_{cr} for conduction and valence band offsets obtained from Eq. (25) for several specific SL geometries. In these estimates we have assumed that the electron effective mass is $0.15m_0$ (typical for ZnSe and other wide gap II–VI semiconductors), and that the heavy-hole mass is five times larger than the electron effective mass — a situation characteristic of many wide-gap semiconductor compounds [13]. It can be seen from Table II that, for the case of $L_w = L_b$, the condition for small-offset rapidly relaxes as the period of the SL gets smaller. And for any fixed SL period, we find further that, as noted above, the narrower the wells of the superlattice, the higher can V be in this regime. Physically, this reflects the fact that the states in a SL move up in energy as the well width shrinks. In the limit of very narrow wells, the ground state of the SL will be pushed up very close to the top of the well. One then expects that this situation will behave as a "small-offset" system. Table II also illustrates the effect of shrinking *barriers* pointed out in the preceding paragraph: i.e., the thinner the barriers, the larger can be the offsets satisfying Eq. (25) even for substantial well thicknesses. In this case the interaction between wells will be large, and thus the subbands broad. This effect of shrinking thicknesses of *either* the wells *or* the barriers can be appreciated from an alternate point of view. Clearly the superlattice will vanish in the limit as we allow either the well thickness or the barrier thickness to approach zero, acquiring in either case bulk-like characteristics. Thus superlattices with ultra-narrow barriers or ultra-thin well widths must necessarily represent the regime of intermediate dimensionality, to which the small-offset concepts automatically apply.

3.5. Effect of effective mass differences in SL layers

In the discussions above, we have not taken into account the consequences of the effective mass difference in the barriers and in the wells. It has been shown that such mass differences alone can also result in subbands, minigaps, and standing waves in SLs (the so-called effective-mass SLs) [14]. It can be shown from

the results of Ref. [14] that the maximum minigap width produced by the mass difference is

$$E_{g,m^*} = \frac{\hbar^2}{m_w^* L^2} \frac{\Delta m^*}{m_b^*}, \tag{28}$$

where L is the SL period, m_w^* and m_b^* are the effective masses in the well and barrier materials, and Δm^* is the mass difference $m_b^* - m_w^*$. Now in semiconductors the effective mass usually scales with the energy gap, so that Δm^* will be automatically accompanied by a band offset, i.e., $\Delta m^*/m_b^* = V/E_g$. This relationship, together with Eq. (28), gives us the opportunity to compare the effects of Δm^* and V. For example, for a SL with $L_w = L_b$, the first minigap width $E_{g,1}$ is $2V/\pi$ (see Eqs. (6) and (9)). We then have

$$\frac{E_{g,m^*}}{E_{g,1}} = \frac{1}{2} \frac{\pi \hbar^2}{m_w^* L^2} \frac{1}{E_g}. \tag{29}$$

Using 100 Å as a representative SL period, $E_g = 2$ eV, and $m^* = 0.15 m_0$, which are typical values for the II–VI semiconductors, we obtain the ratio of E_{g,m^*} over $E_{g,1}$ to be 0.4%. This indicates that the effect of the effective mass difference is exceedingly small compared to that produced by the corresponding band offset. The effect of the mass difference can therefore be ignored in small-offset SLs, as we have done in this presentation.

4. Optical properties of small-offset structures

4.1. Selection rules for optical transitions

4.1.1. Type-I superlattices without wave function mixing

As a basis of comparison, we first summarize the well-known selection rules for optical transitions in type-I SLs with large band offsets. In those structures, subbands at energies below the barriers are strongly localized in the wells by the *confining potentials* of the surrounding barriers. These subbands are indexed by a quantum number (say, N), starting from that closest to the bottom of the well for conduction electrons, and from the top of the well for the holes. The subbands corresponding to the same quantum number have the same symmetry (parity), and this results in the so-called "Dingle rule" [15] for interband optical transitions ($\Delta N = 0$), which largely determine the optical properties of type-I superlattices.

In this section we concentrate on interband transitions in small-offset SLs. We will restrict ourselves to transitions between the conduction band and the *heavy-hole* valence band, because these transitions dominate the interband optical spectra. Since our primary purpose is to present the special properties characterizing the small-offset regime, this simplification has the advantage of keeping the physics in evidence.

To facilitate discussion of these transitions, we again use the designations eN_q and hhN_q for the subband states, where e and hh stand for "electron" and "heavy hole". For example, $e1_1 \rightarrow hh2_1$ refers to the transition from the first conduction subband to the second heavy-hole subband at the zone edge. To obtain the selection rules for optical transitions, we need to evaluate the wave function overlap $\langle \psi_i | \psi_f \rangle$, where ψ_i and ψ_f are the wave functions associated with the initial

and the final states, respectively. Since the origin of the potential profile with respect to z is chosen to be at the center of a well, the SL is symmetric in z, and the wave functions will display a definite parity with respect to the chosen origin. As we shall see, when we consider wave functions obtained in first-order calculation, this will result in a nonvanishing overlap integral only if $\Delta N = 0$.

As a specific example, we consider a type-I superlattice with $L_w = L_b$. With the use of the following orthogonality relations:

$$\frac{2}{L} \int_0^L \cos(n\pi z/L) \cos(m\pi z/L) \mathrm{d}z = \delta_{m,n}, \tag{30a}$$

$$\frac{2}{L} \int_0^L \sin(n\pi z/L) \sin(m\pi z/L) \mathrm{d}z = \delta_{m,n}, \tag{30b}$$

$$\frac{2}{L} \int_0^L \cos(n\pi z/L) \sin(m\pi z/L) \mathrm{d}z = 0, \tag{30c}$$

it is easy to see from Fig. 3 that the wave function overlap $\langle \psi_i | \psi_f \rangle$ translates into the $\Delta N = 0, \Delta q = 0$ selection rule at both $q = 0$ and $q = 1$. This is *exactly* the same selection rule which applies to large band offset superlattices, referred to above (Dingle's rule) — except that in the familiar case of deep wells one does not concern oneself with the value of q, since the subbands are relatively flat and narrow.

The ordering of the $\cos(n\pi z/L)$ and $\sin(n\pi z/L)$ states at the n-th minigap shown in Fig. 3 is specific to $L_w = L_b$ geometry. For $L_w \neq L_b$ the sequence of sine and cosine functions may be different. However, for type-I SLs, the ordering will always be the same for the conduction and the valence subbands, and hence the $\Delta N = 0, \Delta q = 0$ selection rule will always apply, as long as we stay in the first-order approximation.

4.1.2. Type-I superlattices with wave function mixing

When the band offset is very small, the $\Delta N = 0$ selection rule applies very well. However, we have shown in Sec. 3.3 that as the offset increases — although still satisfying the *"smallness"* criteria discussed in Sec. 3.4 — it will eventually bring about admixtures of different subband states. When we calculate the wave function overlap with such admixtures included, we will find that — in addition to the $\Delta N = 0$ selection rules — certain new transitions with $\Delta N \neq 0$ will also be allowed. For instance, we see from Fig. 3 and Table I that for SLs with $L_w = L_b$, transitions hh1→e3 and hh3→e1 become possible at $q = 0$, hh2→e3 and hh3→e2 become allowed at $q = 1$, and so on. To estimate the intensities of these $\Delta N \neq 0$ transitions, we must calculate the actual wave function overlap of the corresponding initial and final states. For example, the transition intensity for hh1→e3 at $q = 0$ is proportional to $|P(\text{hh3} \rightarrow \text{e1})|^2$, where $P(\text{hh3} \rightarrow \text{e1})$ is the wave-function overlap between the hh3 and the e1 states at $q = 0$. Using Eqs. (18) and (19), we have

$$P(\text{hh3} \rightarrow \text{e1}) = \int_0^L \psi_0^{c*} \psi_{2,+}^v \mathrm{d}z = A_0^c A_{2,+}^v \left(\frac{\sqrt{2}V^c}{\pi T_2^c} + \frac{\sqrt{2}V^v}{\pi T_2^v} \right), \tag{31}$$
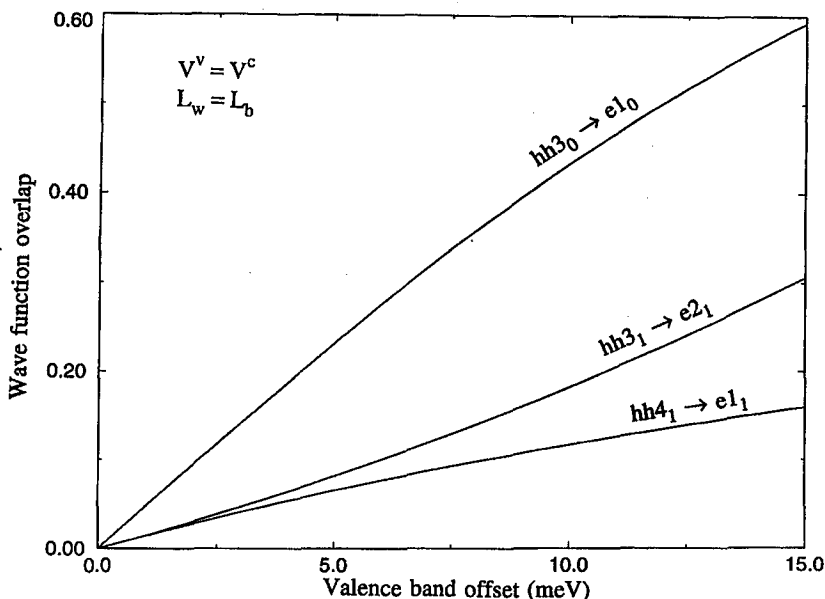
Fig. 4. The wave function overlap as a function of band offset for several "forbidden" ($\Delta N \neq 0$) transitions for a superlattice with $L_w = L_b$, $V^v = V^c$, $m_c^* = 0.15m_0$, and $m_v^* = 5m_c^*$.

where the superscript "c" and "v" refer to the conduction and the valence bands of the SL, respectively. In Fig. 4, we show the wave-function overlap for several transitions induced by wave-function mixing for a SL with $L_w = L_b$, and $V_c = V_b$. It is important to note that the transition probability of the "forbidden" transitions increases with increasing band offset. The results in Fig. 4 are obtained for $V^v = V^c$ and $L_w = L_b$, but our calculations for other combinations of these parameters yield qualitatively very similar behavior [3].

4.1.3. Type-II superlattices

We now consider type-II superlattices. For traditional type-II superlattices with large-band-offsets, there are no simple selection rules because the electrons and the holes are separated in space. However, we will show that for type-II superlattices with small band offsets, selection rules can be found similar to those in type-I structures. In fact, until the band offset becomes very large, there is no qualitative distinction between the type-I and the type-II configurations. This is another characteristic that is unique to the regime of intermediate dimensionality.

As before, we represent the band offsets for such a system by V^c and V^v, respectively. The Fourier coefficients corresponding to the conduction band potential profile may be written, in accord with Eq. (4), as

$$V_n^c = -\frac{V^c}{n\pi} \sin\left(n\pi L_w/L\right). \tag{32}$$

But in a type-II SL (also called the staggered configuration) the layers which act

as wells for conduction electrons constitute barriers for the holes, and vice versa. If we pick the origin in the center of one of the conduction band wells, the origin automatically occurs at the center of a valence band *barrier*. We can handle this formally by describing the offset in the valence band as *negative* $(-V^v)$. In this convention, the Fourier coefficients for the valence band potential profile become

$$V_n^v = -\frac{(-V^v)}{n\pi} \sin\left(n\pi L_w/L\right) = \frac{V^v}{n\pi} \sin\left(n\pi L_w/L\right), \tag{33}$$

where L_w represents layers which correspond to *conduction band wells* (i.e., L_w is physically the same layer in Eq. (32) and Eq. (33)).

Hence V_n^c and V_n^v at the n-th minigap of a type-II superlattice have opposite signs. Recalling that the phase factor θ_n in Eq. (7) is determined by the sign of V_n, we see immediately that $\cos(n\pi z/L)$ and $\sin(n\pi z/L)$ states will have exactly the opposite order for the conduction subbands as they do for the valence subbands. The selection rules for such a SL (to first order, i.e., without wave function mixing) are therefore

$$\Delta N = 1 \tag{34}$$

at $q = 0$ and $q = 1$. The ground state ($N = 1$ at $q = 0$), however, is always an even function. Thus $\Delta N = 0$ continues to apply for the ground state transition (hh1→e1 at $q = 0$).

As in type-I SLs, wave functions in type-II SLs can mix states which have the same parity and wave vector q, and are close in energy. This will again result in many new transitions, not allowed by the $\Delta N = 1$ rule of Eq. (34) or the $\Delta N = 0$ rule for $n = 0$.

4.2. Role of effective mass in optical transitions

Consider an interband transition from an initial state $|i\rangle$ to a final state $|f\rangle$. The transition intensity is then proportional to

$$I \approx |\langle\psi_i|\psi_f\rangle|^2 J_{cv}(E), \tag{35}$$

where $J_{cv}(E)$ denotes the joint density of states [16],

$$J_{cv}(E) = \int_{BZ} 2\frac{dk}{(2\pi)^3}\delta[E_c(k) - E_v(k) - E], \tag{36}$$

and $\int_{BZ}$ indicates integration over the Brillouin zone. It can be shown [17] that $J_{cv}(E)$ is proportional to

$$J_{cv}(E) \approx \left(|\mu_x\mu_y\mu_z|\right)^{1/2}, \tag{37}$$

where μ_i represents the reduced mass along the i-th direction. In our case, electrons moving in the x- and y-directions can be considered "free" and isotropic, so that

$$\mu_x = \mu_y = \text{constant} > 0. \tag{38}$$

What interests us is μ_z (which is determined by the SL geometry) and its effect on J_{cv}. We write μ_z in the form

$$\mu_z = \left(\frac{m_e m_h}{m_e + m_h}\right)_z, \tag{39}$$

where, for interband transition, the masses m_e and m_h are the *minigap masses*. For example, the reduced z-direction mass associated with the transition $hh3_1 \rightarrow e2_1$ is determined by curvatures of the miniband extrema for the final and initial states at the zone edges,

$$\mu_z(hh3_1 \rightarrow e2_1) = \left(\frac{m_e(e2_1)m_h(hh3_1)}{m_e(e2_1) + m_h(hh3_1)} \right)_z . \tag{40}$$

We now discuss the relationship between the effective mass and the optical transitions. First, we recall that $|V_n|$ usually decreases with increasing n, while T_n increases rapidly. Thus, according to Eq. (8), both m_e and m_h will decrease rapidly as we proceed to higher subbands — and so will the reduced mass μ_z. Since the intensity of a particular optical transition is proportional to $\sqrt{|\mu_z|}$, transition intensities will also weaken sharply as n increases, and we will thus limit our study to low-index subbands. Second, the effective mass is much smaller at those minigaps which are closed in first-order (for example, the $n = 2$ minigap when $L_w = L_b$). The reduced mass is then also extremely small at these values of n ($m_n^* \approx m^*(V/T_n)^2$; see Eq. (A15)). It follows automatically that transitions involving such states will be very weak, and will also be ignored in this discussion. Third, we note that m_e is not necessarily much smaller than m_h, since for $\Delta N \neq 0$ transitions they can be associated with different minigaps. Thus in some situations m_e can be close in size to m_h (or even larger). An interesting case here (perhaps the most interesting) involves transitions between electron and hole states having masses of similar magnitude but of *opposite sign*. It can be seen from Eq. (39) that in this case μ_z exhibits a singularity. As a result, one expects a dramatic enhancement of the transition intensity. The physical reason behind the enhancement is that, in such a case, the valence and conduction subbands are approximately parallel as a function of k_z, and hence the joint density of states is greatly increased.

Small-offset SLs also constitute a powerful laboratory for investigating optical transitions in *saddle-point* situations. As was already noted in Eq. (38), the effective masses in the x- and y-directions correspond to free motion, i.e., they are positive quantities. Hence, if $\mu_z > 0$, we have what is termed an M_0 critical point — a true minimum in all directions. If, on the other hand, $\mu_z < 0$, we have, instead, a saddle-point — termed M_1 saddle-point. For example the $hh1_1 \rightarrow e1_1$ transition involves such a saddle-point: it is readily seen from Fig. 3 that both m_e and m_h associated with this transition are negative, so that $\mu_z < 0$. The intensity of the excitonic absorption associated with such a saddle-point is expected to be weak because the saddle-point exciton — since it lies at an energy slightly below that separating the $hh1_1$ and e_1 extrema — automatically occurs within the (wide) miniband. It is thus a resonant state, instead of a bound state, and is therefore characterized by a much weaker transition probability [18, 19].

We emphasize that it is the large width of the minibands — a special characteristic of small-offset SLs — that results in such novel and important role which effective masses play in optical transitions, for two reasons. First, because the minibands are wide, the subband curvature at the zone center and zone edges (which defines the minigap masses) becomes a quantity of physical significance in

these structures. And second, when offsets are small, miniband widths can readily exceed exciton binding energies, resulting in resonant state phenomena (and thus in suppression of optical transitions) such as that described in the preceding paragraph.

4.3. Comparison with experimental results

Using magneto-optical absorption in $ZnSe/Zn_{1-x}Mn_xSe$ small-offset superlattices involving a diluted magnetic semiconductor (DMS) $Zn_{1-x}Mn_xSe$, Dai et al. [2] observed a series of transitions between different conduction and valence subbands, at both the center and at the edge of the SL Brillouin zone. The results in Ref. [2] illustrate many of the features characteristic of small-offset SLs discussed above, and we will compare these experimental observations with the predictions of the NFE analysis.

We will concentrate on the data observed on a SL referred to as "Sample 2" in Ref. [2], which had the following parameters: $x \approx 0.04$, $L_w = L_b = 73$ Å, 10 periods (for additional details, including growth conditions, see Ref. [2]). For Mn concentration $x \approx 0.04$ the resultant band alignments, with strain present, provide band offsets which at zero magnetic field are less than 4 meV (i.e., less than 0.15% of the total band gap) in both the conduction and the valence bands. Thus offsets at the DMS/non-DMS interfaces of the SL are practically negligible in the
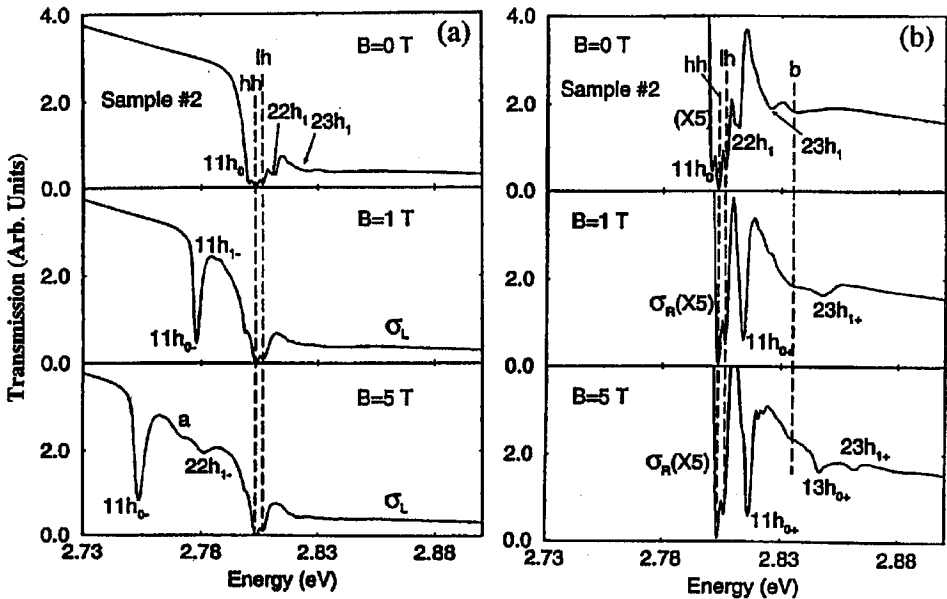

Fig. 5. Absorption spectra for a small-offset SL investigated in Ref. [2] for $\boldsymbol{B} = 0$, 1 and 5 tesla for (a) spin-up orientation, and (b) spin-down orientation. The dashed lines label the peak positions of the light hole ("lh"), the heavy hole ("hh"), as well as one absorption peak "b" from the buffer.

absence of a magnetic field. With the application of a magnetic field, however, large Zeeman splittings of the band edges occur in the DMS layers as a result of exchange interaction between magnetic moments of the Mn ions and band electrons (as discussed in Sec. 2.2). This in turn generates band offsets which are continuously tunable over a range of ± 40 meV in the valence band and ± 10 meV in the conduction band about their respective zero-field values, as the magnetic field is varied from 0 to 5 T for the two spin orientations (see, e.g., Ref. [6]).

Typical absorption spectra for the SL at $B = 0, 1$, and 5 tesla for the σ_L polarization (spin-down transitions) and the σ_R polarization (spin-up transitions) are shown in Figs. 5a and b, respectively. For consistency with Ref. [2], we use the following labeling scheme for the transitions. The label mnh_q indicates the transition from n-th heavy-hole subband (h stands for "heavy") to m-th conduction subband at the SL Brillouin zone center ($q = 0$) or at the zone edge ($q = 1$). Thus the shorthand notation for the transition hh3 $\rightarrow$e2 occurring at the zone edge would be $23h_1$. In addition to the expected $\Delta N = 0$ transitions, one $\Delta N = 1$ and one $\Delta N = 2$ transitions are also present in Fig. 5. These transitions are allowed on the basis of the anticipated relaxation of the $\Delta N = 0$ selection rule as the offsets increase, causing the wave functions to depart from their purely sinusoidal standing wave form. We now discuss these additional transitions.

The band structure and the first-order wave functions at minigaps for a small-offset type-I superlattices with $L_{\rm w} = L_{\rm b}$ were shown in Fig. 3. We have demonstrated that the higher-order wave functions contain admixtures from neighboring subbands of the same parity (see Table I). Due to such wave function mixing, we should expect the following $\Delta N \neq 0$ transitions:

(i) at $q = 0$: $13h_0$ (hh$3_0 \rightarrow$ e1_0), $31h_0$ (hh$1_0 \rightarrow$ e3_0);

(ii) at $q = 1$: $23h_1$ (hh$3_1 \rightarrow$ e2_1), $14h_1$ (hh$4_1 \rightarrow$ e1_1), $41h_1$ (hh$1_1 \rightarrow$ e4_1), $32h_1$ (hh$2_1 \rightarrow$ e3_1).

Here it should be noted that we have limited ourselves to those transitions involving the first three subbands at $q = 0$, and the first four at $q = 1$, since the joint density of states for transitions involving higher subband states rapidly decreases with n.

As discussed in preceding sections, the optical transition intensity is determined by the wave function overlap of the initial and the final states, together with the joint density of states associated with the transition. Table III lists the wave function overlap within one SL period for a series of transitions calculated using the NFE model for Sample 2 for a field of 1 tesla, for spin up subbands. The valence and conduction band offsets corresponding to such a field are 15 meV and 3 meV, respectively [20]. (Note that the NFE model does not explicitly include the magnetic field or the exchange interaction, but formulates the problem in terms of the band offset, regardless of how that offset is produced. In the specific case of DMS/non-DMS SLs, such as Sample 2 of Ref. [2], the offset arises via the Zeeman splitting of the band edges in an applied magnetic field, as discussed in Sec. 2.2, and we then use this band-offset in our NFE model calculation).

Table III also gives the calculated reduced masses μ_z corresponding to these transitions, which can be used as a measure of the joint density of states according to Eq. (37). The intensities of these transitions ($I_{i \rightarrow j}$) were estimated from the

TABLE III

Reduced masses, wave-function overlaps, and transition intensities for various transitions calculated for the SL of Ref. [2].

Transition	μ_z^*	$\langle \psi_i \vert \psi_j \rangle$	$I_{i \to j}^*$
$hh1_0 \to e1_0$	$+1.0$	0.90	1.0
$hh2_0 \to e2_0$	-10^{-3}	0.96	$\mu_z < 0$
$hh3_0 \to e3_0$	$+10^{-3}$	0.88	0.03
$hh3_0 \to e1_0$	$+0.3$	0.59	0.24
$hh1_0 \to e3_0$	$+10^{-3}$	0.59	0.01
$hh1_1 \to e1_1$	-0.08	0.98	$\mu_z < 0$
$hh2_1 \to e2_1$	$+0.06$	0.93	0.26
$hh3_1 \to e3_1$	-0.02	0.90	$\mu_z < 0$
$hh3_1 \to e2_1$	$+0.15$	0.31	0.05
$hh2_1 \to e3_1$	-0.003	0.31	$\mu_z < 0$
$hh4_1 \to e1_1$	-0.23	0.16	$\mu_z < 0$
$hh1_4 \to e4_1$	$+.003$	0.16	0.002

*Reduced mass and intensity are normalized to 1.0 for the $hh1_0 \to e1_0$ transition.

product of the square of the wave-function overlap and the square-root of μ_z (see Eqs. (35) and (37)). These estimated intensities (normalized to the $hh1_0 \to e1_0$ transition) are also shown in Table III, except for those cases where $\mu_z < 0$. As discussed in Sec. 4.2, a negative μ_z is associated with an M_1 saddle-point, so that the intensity of a corresponding transition is expected to be very weak [18, 19].

We begin by considering transitions at the SL Brillouin zone center. From Table III, one can see that the $11h_0$ ($hh1_0 \to e1_0$) transition is the strongest, primarily due to the highest joint density of states. On the other hand, $22h_0$ ($hh2_0 \to e2_0$) and $33h_0$ ($hh3_0 \to e3_0$) transitions should be weak (in spite of the fact that they are both $\Delta N = 0$ transitions), due to the much smaller joint density of states associated with the extremely small minigap for $n = 2$ at zone center (see Figs. 2 and 3). For this reason we expect all transitions involving states $e2_0$ and $e3_0$ to be weak.

Experimentally, it is indeed the case that $11h_0$ is the strongest transition, while $22h_0$ and $33h_0$ are barely observable. In fact, the $22h_0$ and $33h_0$ transition lines cannot be reliably identified from Figs. 5a and b. Dai et al. identified these transitions only after moving them around with magnetic field (see Fig. 13 of Ref. [2]), and with the additional aid of theoretical calculations [2].

On the other hand, Dai et al. have observed the transition $13h_0$ ($hh3_0 \to e1_0$) to be a strong transition. This is again consistent with theoretical prediction. As can be seen from Table III, our NFE model predicts the $13h_0$ transition to be the next to the strongest transition at $q = 0$. This $\Delta N \neq 0$ transition is induced by wave-function mixing, which is small when the band offsets are small. Thus in the

$ZnSe/Zn_{0.96}Mn_{0.04}Se$ SL described above, this transition was not observed at very low magnetic fields. The $13h_0$ transition serves very nicely to illustrate the role of joint density of states in determining transition intensity: the "forbidden" $13h_0$ transition is much stronger than the "allowed" $22h_0$ or $33h_0$ transitions because the density of states associated with the $e1_0$ subband is much higher than that for either $e2_0$ or $e3_0$.

Another expected $\Delta N \neq 0$ transition, $31h_0$ ($hh1_0 \rightarrow e3_0$), is experimentally not observed despite its non-negligible wave function overlap (see Table III), again because of the small density of states of the $e3_0$ state. The peak intensity of this transition is, therefore, expected to be at most comparable to the $22h_0$ and the $33h_0$ transitions, but it lies closer to the region of high opacity, and is thus totally obscured.

Next we discuss the transitions at the SL Brillouin zone edge ($q = 1$). Both $11h_1$ ($hh1_1 \rightarrow e1_1$) and $22h_1$ ($hh2_1 \rightarrow e2_1$) transitions were observed. The intensity of the $11h_1$ transition was found to be much weaker than that of $22h_1$. This is because the $11h_1$ is a *saddle-point* excitonic transition (negative μ_z, see Table III), and its intensity should be weak, as discussed in Sec. 4.2. Note that in Table III, the $11h_1$ transition has the highest wave function overlap of all. Despite this, the absorption peak is barely noticeable, illustrating the role of the sign of μ_z in determining transition intensities.

The most interesting transition observed at $q = 1$ is the $23h_1$ line, involving the $hh3_1$ and $e2_1$ states. This is another wave-function-mixing-induced transition. The estimated intensity shown in Table III indicates that this is a strong transition, which is indeed the case experimentally. The calculated wave function overlap between $hh3_1$ and $e2_1$ states as a function of band offset has been shown in Fig. 4. Judging by the behavior of the overlap, we would not expect to see this $\Delta N = 1$ transition at very low magnetic fields. This is, however, not the case: the transition is clearly seen even for $B = 0$. We suggest that the reason for observing the $23h_1$ transition at these low fields (i.e., at low offsets) can be explained by examining the dispersion of the $e2$ and the $hh3$ subbands in Fig. 3. As can be seen, these subbands are essentially parallel to each other at $q = 1$, which greatly enhances the joint density of states, thus leading to a stronger absorption than for transitions involving opposite curvatures of the E vs. k_z dispersion. Note that Table III shows that the reduced mass associated with this transition is exceptionally large, so that the intensity of this transition should indeed be quite strong.

From the wave-function overlap shown in Table III, one may also expect to see the $14h_1$ ($hh4_1 \rightarrow e1_1$) transition. However, the reduced mass associated with the $14h_1$ transition is again negative, indicating a weak transition based on the arguments given above. Experimentally, this transition was not observed. Finally, all the transitions involving $e3_1$ and $e4_1$ states at $q = 1$ lie very high in energy (calculated energies for these transitions are above 2.88 eV). These transitions are buried in the absorption tail of the buffer layer, and thus were not observed in experiment.

5. Comparison of NFE analytical results with numerical calculations

5.1. Eight-band $k \cdot p$ model and numerical calculations

The results presented in preceding sections were obtained in the NFE approximation, which assumes that the band offset of superlattices under consideration is small, and neglects interactions between bands. The simplicity of this approach has made it possible to formulate the description of small-offset SLs in analytical terms, providing valuable insights into the behavior of semiconductor structures in the regime of intermediate dimensionality. The approach appears to us *a priori* justified for dealing with most wide-gap II–VI and III–V SLs, since the interband interactions are expected to be small in these materials, allowing one to analyze the conduction and the valence bands separately.

Nevertheless, it is important to establish the validity of this approach by demonstrating that the approximations made in the NFE model are indeed justified. We can do this by comparing the results (specifically, wave functions and subband energies) obtained by the analytical NFE method with those obtained by numerical methods from an eight-band $k \cdot p$ model, which accounts for inter-band interactions, and which is valid for offsets of arbitrary value [21]. In this model, the band structure of a SL can be conveniently handled in terms of the so-called *envelope function approximation* [22]. The Schrödinger equation obtained from this approximation is a set of eight coupled second-order differential equations in the variable z, with proper boundary conditions at the interfaces. The equations can be numerically solved using the transfer-matrix method (TMM) algorithm developed by Ram–Mohan et al. [23]. This model satisfies the criteria stated above, and has been recognized in the literature for successfully dealing with semiconductor band structures in general. Comparison of our analytical results with the predictions of such a general model will not only provide a test for the applicability of our results in the small offset limits, but will also serve to establish the range of applicability of these results, i.e., how large must the offset become for the analytical results to fail.

In the eight-band $k \cdot p$ model, the interactions between the Γ_6 (conduction band), Γ_8 (valence band), and Γ_7 (spin-orbit-split band) are treated exactly, and the interactions between these bands and the more remote higher bands are included up to order k^2. For describing the well layers of the SL, we have chosen the parameters of ZnSe [2], since this semiconductor is representative of wide-gap II–VI materials which are of direct interest to our research group. To describe the barriers, we have chosen the same parameters as those used for the wells except for the band gap, which was adjusted to introduce the desired amount of band offset in the conduction and valence bands. The zero-energy point is chosen to lie at the top of the valence band of the well material, and the band gap of the well material is taken as 2.803 eV (the energy gap of ZnSe). In the NFE model we use the effective masses $m_e^* = 0.14$, and $m_{hh}^* = 0.73$, which correspond exactly to the values of m_e^* and m_{hh}^* obtained from the eight-band $k \cdot p$ model for ZnSe. Our purpose, however, is not to attempt a rigorously accurate description of ZnSe or any other specific material, but only to compare the predictions of the NFE and of the numerical multi-band calculation for identical structures. For the same reason, we

do not include either the strain or the magnetic parameters given by Ref. [2] in our 8-band model calculation. We only focus on the energy levels and wave functions for a given band offset value, which allows us to make direct comparisons of the numerical calculations with the results of the NFE model obtained for the same value of the offset.

As a test case for comparing the NFE and the 8-band numerical calculations, we have chosen a type-I SL comprised of 50 Å wells and 50 Å barriers. At these dimensions the structure clearly displays all features characteristic of SLs: localization of states deep in the well, effects of confinement of subband energies, and subband interactions across barriers. Such dimensions are also typical for structures used in experiments. The choice of equal well and barrier thicknesses ($L_w = L_b$) corresponds to the situation examined explicitly in previous sections, so that we can make reference to those results in discussing the numerical calculations.

5.2. Comparison of NFE and TMM results
5.2.1. Wave functions

Correct calculation of wave functions at subband extrema is crucial, because this will determine the wave function overlap associated with specific optical transitions. We therefore give special attention to comparing the wave functions predicted by the NFE model and by the 8-band model using the transfer-matrix method.
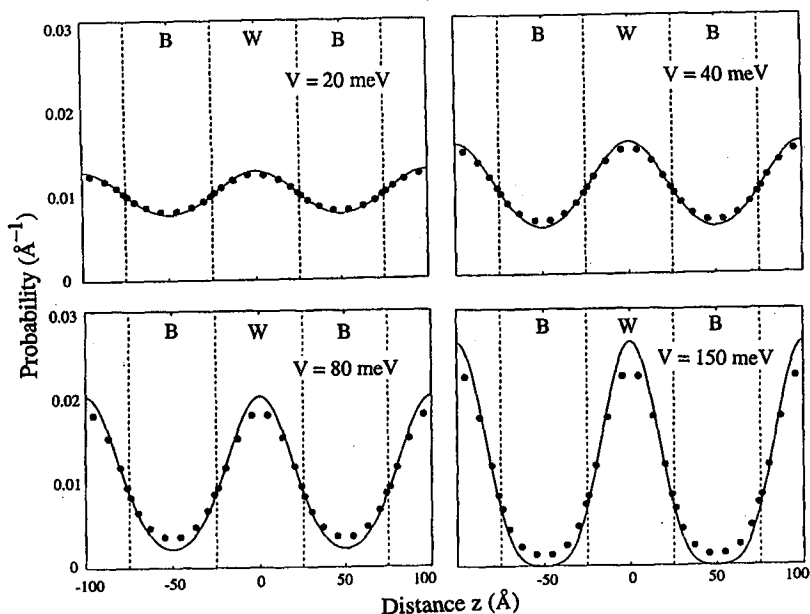

Fig. 6.   Probability distribution $|\Psi(z)|^2$ as a function of position z (in Å) for the zone-center state $e1_0$, calculated by 8-band $k \cdot p$ model (points) and by the NFE model (solid curve) for several values of the band offset V, as indicated in the figure.

We begin by examining the progression of $|\psi(e1_0)|^2$ for a series of offsets, as shown in Fig. 6. In this figure — and in those that follow — the continuous curve represents the NFE calculation, and the 8-band numerical calculation results are given by points. The electron probability $|\psi|^2$ is plotted as a function of z, with $z = 0$ corresponding to the center of one of the wells. The wave function ψ is normalized so that $|\psi|^2$ integrates to unity over one SL period.

We see in Fig. 6 that the agreement of $|\psi(e1_0)|^2$ calculated by both methods is excellent for offset values up to at least 40 meV. At offset values of 80 meV and 150 meV, the NFE wave functions begins to deviate from the 8-band calculation. However, the agreement is in general still quite good even at these values of band offset. We use this occasion to recall that the oscillatory behavior of $\psi(e1_0)$ as a function of z is itself a result of admixture from nearby states, arising from second-order perturbation. The amount of admixture is proportional to V (see Table I), and Fig. 6 thus serves to illustrate the gradual transformation of the SL from 3D to a 2D medium: when $V = 0$, the wave functions revert to their bulk characteristics, with no localization.
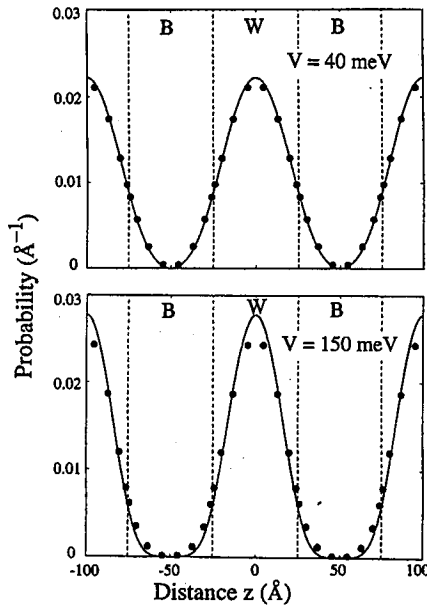

Fig. 7. Probability distribution $|\Psi(z)|^2$ as a function of position z (in Å) for the zone-edge state $e1_1$, calculated by 8-band $\mathbf{k} \cdot \mathbf{p}$ model (points) and by the NFE model (solid curve) for several values of the band offset V, as indicated in the figure.

We now consider $|\psi(e1_1)|^2$, shown as a function of z in Fig. 7. The agreement between NFE and the 8-band numerical calculation is again excellent, better in fact than for the $e1_0$ state. This is to be expected, since in examining $\psi(e1_0)$ our attention was focused on the oscillatory *admixture* (primarily from the $e3_0$ state;
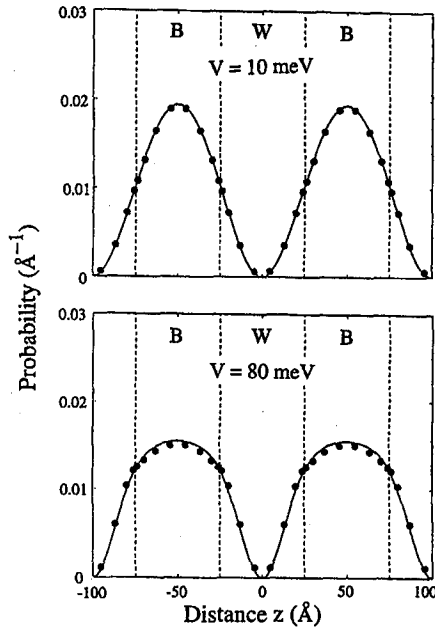
Fig. 8. Probability distribution $|\Psi(z)|^2$ as a function of position z (in Å) for the zone-edge state $e2_1$, calculated by 8-band $\mathbf{k} \cdot \mathbf{p}$ model (points) and by the NFE model (solid curve) for several values of the band offset V, as indicated in the figure.

see Table I) arising from second-order perturbation, while $\psi(e1_1)$ is dominated by the first-order contribution (the $\cos(\pi z/L)$ dependence). Here it is interesting to note that, as V increases, $|\psi(e1_0)|^2$ and $|\psi(e1_1)|^2$, become more and more like one another. This provides insight into an important physical process: as V becomes larger, the $n = 1$ subband becomes increasingly narrow and flat, gradually losing its dependence on q. The states $e1_0$ and $e1_1$, which represent the extrema of this subband at $q = 0$ and $q = 1$, must eventually become indistinguishable — and we indeed see this happening as V becomes large.

We now present the results for the state $e2_1$ (see Fig. 8). Note, first, that $|\psi(e2_1)|^2$ varies as $\sin^2(\pi z/L)$, i.e., that the parity sequence of the standing waves predicted by the 8-band model is the same as that of the NFE model, displayed in Fig. 3. This feature — the agreement of parity between NFE and 8-band models — survives for all states examined. Returning to Fig. 8, we note the similarity of the two calculations even when the wave function is deformed by admixtures, as shown for $V = 80$ meV in the lower panel.

The comparison of wave functions at higher subbands calculated by NFE and 8-band model, such as $|\psi(e2_0)|^2$, $|\psi(e3_0)|^2$ and $|\psi(e3_1)|^2$, is similarly good. Since the agreement of wave functions is actually expected to improve as we test increasingly higher-lying subbands, we will stop our wave function comparisons for the conduction band, and will proceed to examine wave functions in the valence band.
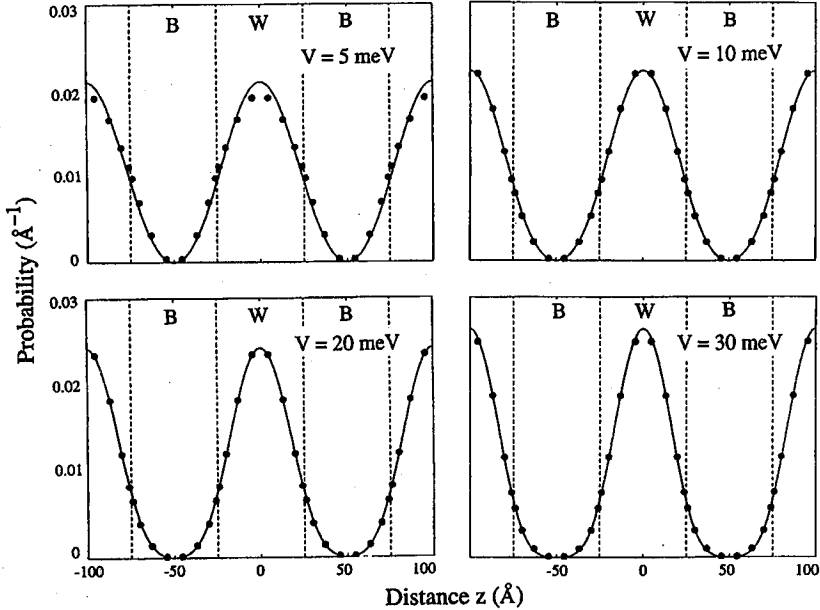
Fig. 9.   Probability distribution $|\Psi(z)|^2$ as a function of position z (in Å) for the zone-edge state $hh1_1$, calculated by 8-band $k \cdot p$ model (points) and by the NFE model (solid curve) for several values of the band offset V, as indicated in the figure.

In Fig. 9 we compare the probability distributions $|\psi(hh1_1)|^2$ calculated by NFE and by the 8-band model. The agreement between the two results is once more rather striking. Although this may appear qualitatively repetitious after discussing the comparison for the state $e1_1$ (and it certainly is so in the context of the NFE approximation), making the comparison with an exact calculation is in this case necessary because of the special complexities characterizing the heavy-hole band. The latter band lies close to the light-hole and the Γ_7 bands, and one must therefore test for the effect of interactions with those bands. The agreement between the NFE calculation (which does not include these interactions) and the 8-band numerical calculations (which accounts for them exactly) demonstrates that, at least within the offset limits tested, heavy holes can be satisfactorily described in terms of the free-particle model.

5.2.2. Subband energies and minigaps

We calculated the energies at subband extrema (i.e., for $q = 0$ and $q = 1$) by the NFE and the 8-band $k \cdot p$ models for a 50 Å/50 Å superlattice, for offsets of 10 meV in both the conduction and the valence bands. The valence band well is thus at 0, the conduction well at 2.803 eV, the conduction band barrier at 2.813 eV, and valence band barrier at −0.010 eV. The results are presented in Table IV. The energies were actually calculated to an accuracy of 0.001 meV and were rounded off to 0.1 meV in the table. The values of the minigaps were rounded off to 0.01 meV.

Examining Table IV, we note that the agreement between the NFE and the results obtained from the 8-band model is in general quite good for the lower states (within 2 meV), but the two calculations begin to depart one from the other for higher subbands. This is clearly noticeable for subbands $e3_1$ and higher in the conduction band. The fact that the NFE result is systematically higher than the value calculated from the 8-band model offers an important insight into a mechanism not previously considered. We ascribe this deviation to nonparabolicity of the E vs. k relationship, which is very precisely accounted for in the eight-band model, but is not present in the NFE model.

TABLE IV

Energies (in meV) at subband extrema ($q = 0$ and $q = 1$) calculated by NFE and TMM models for a 50 Å / 50 Å SL with an offset of 10 meV in both CB and VB.

Subband extremum	TMM calculation*	NFE calculation*
$e1_0$	$E_g^w + 4.8$	$E_g^w + 4.8$
$e1_1$	$E_g^w + 29.7$	$E_g^w + 28.7$
$e2_1$	$E_g^w + 36.0$	$E_g^w + 35.1$
$e2_0$	$E_g^w + 113.0$	$E_g^w + 113.0$
$e3_0$	$E_g^w + 113.3$	$E_g^w + 113.3$
$e3_1$	$E_g^w + 236.0$	$E_g^w + 247.5$
$e4_1$	$E_g^w + 238.0$	$E_g^w + 249.6$
$hh1_0$	-4.0	-4.0
$hh1_1$	-6.4	-6.0
$hh2_1$	-12.7	-12.3
$hh2_0$	-24.0	-24.0
$hh3_0$	-25.2	-25.2

*The well energy gap, E_g^w, is 2.803 eV.

A feature that clearly emerges from Table IV in both the NFE and the TMM results is that, when the offsets are small, most of the states lie at energies above the barriers. This is clearly evident in the case of conduction band, where only the $e1_0$ state is in the well, with most of the lowest ($N = 1$) subband and all higher subbands above the barrier. The same will be true of the valence band for smaller offsets than that arbitrarily chosen for calculations in Table IV. It is for this reason that states in small-offset SLs resemble in many ways *above-barrier* states in conventional SLs [24, 25]. In both these cases the states are localized as standing waves formed by Bragg reflection, rather than by direct confinement in the SL wells [26].

We now consider the minigaps calculated by the two methods, as listed in Table V. The agreement is excellent, even for the higher subbands, where the above-mentioned nonparabolicity effects begin to be important. Note also that the

TABLE V

Minigap widths (in meV) calculated by NFE and TMM models for a 50 Å / 50 Å SL with an offset of 10 meV in both CB and VB.

Minigap between	TMM calculation	NFE calculation
$e1_1$ and $e2_1$	6.31	6.37
$e2_0$ and $e3_0$	0.23	0.23
$e3_1$ and $e4_1$	1.99	2.12
$e4_0$ and $e5_0$	0.06	0.06
$hh1_1$ and $hh2_1$	6.30	6.37
$hh2_0$ and $hh3_0$	1.24	1.22

lowest minigaps in both bands, (i.e., those between $e2_1$ and $e1_1$ and between $hh2_1$ and $hh1_1$) are very close to one another. This is as it should be since, according to Eqs. (4) and (6), the minigap only depends on the band offset V (which in this case is the same in both bands). On the other hand, minigaps between $e3_0$ and $e2_0$, and between $hh3_0$ and $hh2_0$ are closed in first-order calculation for $L_w = L_b$ ($V_n = 0$ for $n = 2$). The second-order perturbation result for the minigap, given by Eq. (A15), depends on both V and m^*. It can be seen from Eq. (A15) that the ratio of $E_{g,2}^v/E_{g,2}^c$ would equal m_{hh}^*/m_e^*, which is 5.2 for the parameters used. The minigap ratios obtained by NFE and the 8-band model are, respectively, 5.26 and 5.50. The agreement of the NFE result with m_{hh}^*/m_e^* is of course not surprising, but the value obtained from the 8-band model at this sensitive point is significant in that it confirms the validity of the second-order treatment (which is expected to be more sensitive to approximations), and of the analytical results arising from it.

As energies increase, so do the subtleties of calculation which enter into the values of the minigaps. The fact that the two methods predict results which are very close for $E_{g,3}^c$ and $E_{g,4}^c$ serves as further confirmation of the accuracy of the NFE model and, conversely, allows us to use NFE to identify mechanisms that are behind the exact numerical results.

6. Concluding remarks

In this paper we have explored physical phenomena which occur when a semiconductor superlattice just begins to form, i.e., when the quantum wells which determine the superlattice are very shallow. A distinct feature of this regime of "intermediate dimensionality" is that, when band offsets are small, the SL wave functions are standing waves, localized by Bragg reflections rather than by confinement in the wells.

We have shown that this region is characterized by a large number of novel optical effects. For example, because of their extremely broad subbands, small-offset SLs allow us to distinguish between transitions occurring at the center of the Brillouin zone ($q = 0$) and at its edges ($q = 1$). Another very striking feature of the SLs in this regime is that, due to the wave function mixing of different subband states, the traditional $\Delta N = 0$ selection rule is relaxed, and many new $\Delta N \neq 0$

transitions will occur. We also discussed the opportunity which these small offset systems provide of investigating the role of the effective mass (its size, sign, and topology, such as the saddle-point) in determining the strengths of various optical transitions.

The theoretical model we used is the nearly free electron model, and the results are analytical and very simple. The validity of these results has been verified by comparing them with the numerical calculations from a 8-band $k \cdot p$ model. These comparisons have shown that our analytical results apply well even at fairly large band offsets. At the same time, the analytical results — by their transparent simplicity — provide valuable insights and understanding for SL behavior obtained via rigorous but complicated numerical calculations.

Appendix A
Formation of minigaps for $V_n = 0$

We have shown in Sec. 3.1 (see Eq. (6)) that first-order perturbation analysis gives the minigap width of small offset SLs as

$$E_{g,n} = 2|V_n|, \tag{A1}$$

where V_n is defined by Eq. (3). It is easy to see from Eq. (4) that, depending on the relationship of L_w to L, V_n can vanish for certain n. The first-order perturbation minigap will then also vanish, and second-order perturbation theory must be applied to obtain expressions for minigaps, wave functions, and effective masses at $k_z = \pm n\pi/L$. Before we examine the second-order perturbation approach for such cases, we will discuss the conditions necessary for V_n to vanish for the case of SLs with a rectangular potential profile. The Fourier coefficients V_n for such SLs are

$$V_n = -\frac{V}{n\pi} \sin(n\pi L_w/L) \qquad \text{for} \qquad n = 1, 2, 3, \ldots \tag{A2}$$

Setting $V_n = 0$ then implies that $nL_w/L = m$, where m and n are integers. Hence there will exist values of n for which V_n will vanish whenever L_w/L is a ratio of two integers. For example, V_n will vanish for all even n when $L_w = L/2$ ($L_w = L_b$); it will vanish for $n = 3, 6, 9, \ldots$ when $L_w = L/3$ or $L_w = 2L/3$; etc.; and in general, the thinner the well or the barrier, the higher will be the value of n for which V_n first vanishes.

For those conditions when V_n vanishes, we need to use second-order perturbation analysis to obtain the wave functions, minigap widths, and effective masses. The wave functions will be determined by linear combinations of the basis functions

$$|n\rangle = \frac{1}{\sqrt{L}} \exp(in\pi z/L), \qquad |-n\rangle = \frac{1}{\sqrt{L}} \exp(-in\pi z/L) \tag{A3}$$

in the form

$$\psi = A|n\rangle + B|-n\rangle, \tag{A4}$$

where A and B are constants. Following degenerate perturbation theory, we find the system of equations which have to be solved

$$(E - E_k^{(0)} - H_{kk})A - H_{kk'}B = 0 \tag{A5a}$$

$$-H_{kk'}^* A + (E - E_{k'}^{(0)} - H_{k'k'})B = 0. \tag{A5b}$$

The resulting determinant which must be solved is then

$$\begin{vmatrix} E - E_k^{(0)} - H_{kk} & -H_{kk'} \\ -H_{kk'}^* & E - E_{k'}^{(0)} - H_{k'k'} \end{vmatrix} = 0, \tag{A6}$$

where

$$H_{kk} = \sum_{m \neq \pm n} \frac{|\langle n|V|m \rangle|^2}{T_n - T_m}, \tag{A7a}$$

$$H_{k'k'} = \sum_{m \neq \pm n} \frac{|\langle -n|V|m \rangle|^2}{T_n - T_m}, \tag{A7b}$$

and

$$H_{kk'} = \sum_{m \neq \pm n} \frac{\langle n|V|m \rangle \langle m|V|-n \rangle}{T_n - T_m}. \tag{A7c}$$

Here $T_s = (\hbar s \pi)^2/(2m^* L^2)$, where s stands for n or m. It is easy to show that $H_{kk} = H_{k'k'}$, and $E_k^{(0)} = E_{k'}^{(0)} = T_n$. Thus, the solution of Eq. (A6) is

$$E_{n,\pm} = T_n + H_{kk} \pm |H_{kk'}|, \tag{A8}$$

where $E_{n,+}$ and $E_{n,-}$ refer to the two energy extrema associated with the n-th minigap. The wave functions for the "upper" and "lower" energy states at such a minigap are

$$\Psi_{n,+} = \frac{2Ae^{-i\theta_n}}{\sqrt{L}} \cos{(n\pi z/L, +\theta_n)}, \ \Psi_{n,-} = \frac{2Aie^{-i\theta_n}}{\sqrt{L}} \sin{(n\pi z/L + \theta_n)}, \tag{A9}$$

where the phase factor θ_n is determined by $e^{2i\theta} = H_{kk'}/|H_{kk'}|$.

The width of the n-th minigap is thus

$$E_{g,n} = 2|H_{kk'}|. \tag{A10}$$

For the case of a rectangular potential $H_{k,k'}$ is real, so the wave functions are $\cos(n\pi z/L)$ and $\sin(n\pi z/L)$. Which of these is associated with $E_{n,+}$ and which with $E_{n,-}$ is determined by the phase factor θ_n, and that depends on the SL geometry (i.e., on L_w/L).

As an example, we first consider a superlattice with wells and barriers of equal width, $L_w = L_b$, i.e., $L = 2L_w$. Equation (9) shows that V_n (and thus the first-order minigaps) vanish for all even values of n. We will see below, however, that minigaps for this geometry remain finite for even values of n when calculations are carried out to second order.

As an illustration, we derive the wave functions and the minigap width for $n = 2$. Essentially, we need only to calculate $H_{kk'}$, defined by Eq. (A7c). By using Eq. (3), it can be shown that

$$H_{kk'} = \frac{V_1^2}{T_2} + \frac{2V_1^* V_3}{T_2 - T_4} + \frac{2V_3^* V_4}{T_2 - T_6} + \frac{2V_3^* V_5}{T_2 - T_8} + \cdots, \tag{A11}$$

where $V_m = \langle n|V|n'\rangle$, and $m = (n' - n)/2$ (m is an integer). Inserting Eq. (9) into (A11) yields

$$H_{kk'} = \frac{V^2}{\pi^2 T_2}\left[1 + \frac{2}{(1\times 3)^2} + \frac{2}{(3\times 5)^2} + \frac{2}{(5\times 7)^2} + \ldots\right]$$

$$= \frac{V^2}{\pi^2 T_2}\left[1 + 2\sum_{n'}\frac{1}{[(2n'-1)(2n'+1)]^2}\right]. \tag{A12}$$

It can be proven that

$$1 + 2\sum_{n'}\frac{1}{[(2n'-1)(2n'+1)]^2} = \frac{\pi^2}{8}. \tag{A13}$$

Using this result in Eq. (A12), we finally obtain

$$H_{kk'} = \frac{V^2}{8T_2}. \tag{A14}$$

The minigap given in Eq. (A10) can thus be expressed as

$$E_{g,2} = 2|H_{kk'}| = \frac{V^2}{4T_2}, \tag{A15}$$

which is extremely small (smaller than $E_{g,n}$ for $n > 2$ when V_n does not vanish), but nevertheless finite.

Finally, the expressions for the wave functions of the two states ($E_{2,\pm} = T_2 \pm V^2/(8T_2)$) associated with this gap are as follows (from Eq. (A9)):

$$\psi_{2,+} = \frac{\sqrt{2}}{\sqrt{L}}\cos(2\pi z/L), \qquad \psi_{2,-} = \frac{\sqrt{2}}{\sqrt{L}}\sin(2\pi z/L). \tag{A16}$$

Following the same procedure, one can derive the wave functions and minigap widths for $n = 4, 6, 8\ldots$. Figure 3 shows the subband structure with proper order of the wave functions at the minigaps for the case of $L_w = L_b$.

Appendix B
Second order effective masses at subband extrema

Using the reduced Brillouin zone, we note that the E vs. k dependence in the immediate proximity of each minigap can be approximated by a parabolic relationship

$$E = \frac{\hbar^2 k^2}{2m_n^*}, \tag{B1}$$

where m_n^* is the effective mass associated with the n-th minigap, defined as

$$m_n^* = \frac{\hbar^2}{d^2 E/dk^2}, \tag{B2}$$

and evaluated at each subband extremum. Thus, m_n^{*-1} is related to the curvature of the $E(k)$ vs. k curve *at* the n-th minigap. Where the curvature $d^2 E/dk^2$ is large, the mass is small, while a small curvature (relatively flat extremum) implies a large mass.

We have seen earlier that there exist instances when the n-th minigap, $E_{g,n}$, vanishes to first order for certain values of n (e.g., for all even n in the case $L_w = L_b$ examined above). We have shown in Appendix A that in actuality the minigaps at these values of n are finite, but exceedingly small. We will now analyze the effective masses characterizing minigaps which are closed in first-order perturbation.

In order to derive the expression for the effective mass (i.e., to determine the curvature of the subband at a given zone boundary), we must examine points which are slightly displaced from that zone boundary (i.e., from $k = \pm n\pi/L$). We represent these points by

$$k = \frac{n\pi}{L}(1 + \Delta), \qquad k' = -\frac{n\pi}{L}(1 - \Delta), \tag{B3}$$

where Δ is assumed to be a small quantity (i.e., $\Delta \ll 1$). Again, the corresponding wave function will be a linear combination of the two states corresponding to k and k':

$$\psi = A\psi_k^{(0)} + B\psi_{k'}^{(0)}. \tag{B4}$$

We now again have to solve the system of equations (A5) and (A6), but using wave vectors in Eq. (B3). The solution is

$$E = \frac{1}{2}(E_k^{(0)} + E_{k'}^{(0)} + H_{kk} + H_{k'k'})$$

$$\pm \frac{1}{2}[(H_{kk} - H_{k'k'} + E_k^{(0)} - E_{k'}^{(0)})^2 + |H_{kk'}|^2]^{1/2}, \tag{B5}$$

where

$$E_k^{(0)} = T_n(1 + \Delta)^2, \qquad E_{k'}^{(0)} = T_n(1 - \Delta)^2, \tag{B6}$$

and

$$H_{kk} = \sum_{m_\Delta \neq \pm n} \frac{\langle k|V|m_\Delta\rangle\langle m_\Delta|V|k\rangle}{T_n(1 + \Delta)^2 - T_{m_\Delta}}. \tag{B7}$$

The notation $|m_\Delta\rangle$ indicates those states which differ from $k = (n\pi/L)(1 + \Delta)$ by $\pm 2\pi/L, \pm 4\pi/L, \pm 6\pi/L, \pm \ldots$.

We find similar expressions for $H_{k'k'}$

$$H_{k'k'} = \sum_{m_\Delta \neq \pm n} \frac{\langle k'|V|m_\Delta\rangle\langle m_\Delta|V|k'\rangle}{T_n(1 + \Delta)^2 - T_{m_\Delta}} \tag{B8}$$

and for $H_{kk'}$

$$H_{kk'} = \sum_{m_\Delta \neq \pm n} \frac{\langle k|V|m_\Delta\rangle\langle m_\Delta|V|k'\rangle}{T_n(1 + \Delta)^2 - T_{m_\Delta}}. \tag{B9}$$

In the above derivation, we have made use of the fact that

$$T_n(1 + \Delta^2) = \frac{1}{2}[T_n(1 + \Delta)^2 + T_n(1 - \Delta)^2]. \tag{B10}$$

The actual derivation of the above matrix elements is quite tedious, since the states involved are shifted away from the Brillouin zone boundaries ($k = \pm n\pi/L$) by the increment Δ. The final results for the quantities $H_{kk}, H_{kk'}$, and $H_{k'k'}$

contain terms involving all orders of Δ. Since $\Delta \ll 1$, we keep terms only up to order Δ^2. By using (B2) and the relation

$$\frac{\mathrm{d}^2 E}{\mathrm{d}k^2} = \frac{\mathrm{d}^2 E}{\mathrm{d}\Delta^2}\frac{\mathrm{d}^2\Delta}{\mathrm{d}k^2} = \left(\frac{L}{2\pi}\right)^2 \frac{\mathrm{d}^2 E}{\mathrm{d}\Delta^2}. \tag{B11}$$

we get

$$m_n^* \equiv \frac{m^*|H_{kk'}|}{2T_n} = \frac{m^* E_{gn}}{4T_n}, \tag{B12}$$

where we have used Eq. (A10). As in the first-order calculation, the effective mass is again proportional to the minigap width. But since that width is now very small, the magnitude of the effective mass is accordingly much smaller than the masses associated with those minigaps which are open in first-order.

Acknowledgments

References

[1] G. Bastard, *Wave Mechanics Applied to Semiconductor Heterostructures*, Halsted, New York 1988.

[2] N. Dai, L.R. Ram-Mohan, H. Luo, G.L. Yang, F.C. Zhang, M. Dobrowolska, J.K. Furdyna, *Phys. Rev. B* **50**, 18153 (1994).

[3] L.A. Lewandowski, Ph.D. Dissertation, University of Notre Dame, 1995 (unpublished).

[4] See, e.g., *The Fermi Surface*, Eds. W.A. Harrison, M.B. Webb, Wiley, New York 1960.

[5] A. Twardowski, T. Dietl, M. Demianiuk, *Solid State Commun.* **48**, 845 (1983).

[6] See, e.g., J.K. Furdyna, *J. Appl. Phys.* **64**, R29 (1988).

[7] N. Dai, H. Luo, F.C. Zhang, N. Samarth, M. Dobrowolska, J.K. Furdyna, *Phys. Rev. Lett.* **67**, 3824 (1991).

[8] W.C. Chou, A. Petrou, J. Warnock, B.T. Jonker, *Phys. Rev. Lett.* **67**, 3820 (1991).

[9] E. Deleporte, J.M. Berroir, G. Bastard, C. Delalande, J.M. Hong, L.L. Chang, *Phys. Rev. B* **42**, 5891 (1990).

[10] S. Raimes, *The Wave Mechanics of Electrons in Metals*, North-Holland, Amsterdam 1961, p. 205.

[11] H. Jones, *The Theory of Brillouin Zones and Electronic States in Crystals*, North-Holland, Amsterdam 1960, p. 24.

[12] J. Fang, D. Lu, *Solid State Physics*, Science and Technology Publishing Co., Shanghai 1980, p. 209.

[13] *Landolt-Bornstein Numerical Data and Functional Relationships in Science and Technology*, Group III, Vol. 17, Ed. O. Madelung, Springer, Berlin 1982.

[14] A. Sasaki, *Phys. Rev. B* **30**, 7016 (1984).

[15] R. Dingle, W. Wiegmann, C.H. Henry, *Phys. Rev. Lett.* **33**, 827 (1974).

[16] F. Wooten, *Optical Properties of Solids*, Academic Press, New York 1972, Ch. 5, Sec. 5.3.

[17] F. Bassani, G.P. Parravicini, *Electronic States and Optical Transitions in Solids* Pergamon Press, New York 1975.

[18] H. Chu, Y-C. Chang, *Phys. Rev. B* **36**, 2946 (1987).

[19] B. Deveaud, A. Chomette, F. Clerot, A. Regreny, J.C. Mann, R. Romestain, G. Bastard, H. Chu, Y.-C. Chang, *Phys. Rev. B* **40**, 5802 (1989).

[20] N. Dai, Ph.D. Dissertation, University of Notre Dame, 1993 (unpublished).

[21] C.R. Pidgeon, R.N. Brown, *Phys. Rev.* **146**, 575 (1966); see also W. Leung, L. Liu, *Phys. Rev. B* **8**, 3811 (1973); also Ref. [2], above.

[22] G. Bastard, *Phys. Rev. B* **24**, 5693 (1981).

[23] L.R. Ram-Mohan, K.H. Yoo, R.L. Aggarwal, *Phys. Rev. B* **38**, 6151 (1988).

[24] F.C. Zhang, N. Dai, H. Luo, N. Samarth, M. Dobrowolska, J.K. Furdyna, L.R. Ram-Mohan, *Phys. Rev. Lett.* **68**, 3220 (1992).

[25] F.C. Zhang, H. Luo, N. Dai, N. Samarth, M. Dobrowolska, J.K. Furdyna, *Phys. Rev. B* **47**, 3806 (1993).

[26] H. Luo, J.K. Furdyna, *Mod. Phys. Lett. B* **7**, 299 (1993).